

# The significance of the largest scale CMB fluctuations in WMAP

Angélica de Oliveira-Costa<sup>1</sup>, Max Tegmark<sup>1</sup>, Matias Zaldarriaga<sup>2</sup> & Andrew Hamilton<sup>3</sup>

<sup>1</sup>*Dept. of Physics & Astronomy, University of Pennsylvania, Philadelphia, PA 19104, USA*  
*angelica@higgs.hep.upenn.edu*

<sup>2</sup>*Dept. of Physics, Harvard University, Cambridge, MA 02138, USA and*

<sup>3</sup>*JILA & Dept. of Astrop. & Planetary Sciences, U. Colorado, Boulder, CO 80309, USA*

(Dated: Submitted to Phys. Rev. D. July 15 2003, revised Oct. 14 2003 - still no referee report.)

We investigate anomalies reported in the Cosmic Microwave Background maps from the Wilkinson Microwave Anisotropy Probe (WMAP) satellite on very large angular scales and discuss possible interpretations. Three independent anomalies involve the quadrupole and octopole: 1) The cosmic quadrupole on its own is anomalous at the 1-in-20 level by being low (the cut-sky quadrupole measured by the WMAP team is more strikingly low, apparently due to a coincidence in the orientation of our Galaxy of no cosmological significance); 2) The cosmic octopole on its own is anomalous at the 1-in-20 level by being very planar; 3) The alignment between the quadrupole and octopole is anomalous at the 1-in-60 level. Although the *a priori* chance of all three occurring is 1 in 24000, the multitude of alternative anomalies one could have looked for dilutes the significance of such *a posteriori* statistics. The simplest small universe model where the universe has toroidal topology with one small dimension of order half the horizon scale, in the direction towards Virgo, could explain the three items above. However, we rule this model out using two topological tests: the *S*-statistic and the matched circle test.

## I. INTRODUCTION

It is common in science that when measurements are improved, old questions are answered and new ones are raised. In this sense, history has repeated itself with the spectacular new Cosmic Microwave Background (CMB) results from the Wilkinson Microwave Anisotropy Probe (WMAP) [1]. The WMAP power spectrum results [2] are in near-perfect agreement with the cosmological concordance model in *vogue* (see, *e.g.*, [3, 4]), but have sent cosmologists scrambling to figure out what to make of the detection of a high reionization optical depth and hints of a running spectral index [5, 6]. The “near-perfect” caveat above refers to the surprisingly low amplitude of the observed CMB quadrupole, reflecting a lack of large-angle correlations significant at about the 99.9% level [2, 5], *c.f.* [7, 12]. The low quadrupole amplitude seen by WMAP was also observed by COBE/DMR (see, *e.g.*, [8], [9] and references therein), but only now, with the large WMAP frequency coverage and the low detector noise, has it become possible to show that this low CMB quadrupole is not significantly affected by Galactic emission [10–12]. Compounding the puzzle, anomalies related to the WMAP octopole were reported in [11].

During years, the suppression of large-scale power (sometimes referred in the literature as a *cutoff*), have been used by many authors as evidence for a “small universe” with non-standard topology (see, *e.g.*, [13–17]). If so, the conventional explanation is that such suppression could be caused by the fact that we live in a Universe with compact topology, in which power on scales exceeding the fundamental cell size is suppressed – see [18] and references therein for a review of this subject. If the low multipole behavior is caused by our universe having  $T^1$  [19] compact topology with one dimension small relative to the horizon scale, then the large scale power would

be suppressed in this particular spatial direction as illustrated in Figure 1. Another possibility is hyperspherical topology corresponding to a closed universe [20, 21].

Another class of explanations that have been proposed involve modifying the inflationary picture to introduce a cutoff in the primordial power spectrum [22–26], perhaps linked to the spatial curvature scale [21] or string physics [27]. There is also a class of models that explain the lower multipole values by invoking the existence of fluctuations in a quintessence-like scalar field which can introduce features on scales comparable to the present day Hubble radius [28]. The difficulty here is to cancel the large integrated Sachs-Wolfe anisotropy associated with a high vacuum energy density.

The goal of this paper is to go back to the WMAP data and investigate these large-scale anomalies in greater detail, to clarify what anomalies (if any) are statistically significant and to look for other signatures of non-standard topologies. The rest of this paper is organized as follows. In Section II, we compute the significance of the low quadrupole, the planar octopole and their alignment. In Section III A, we simulate a grid of small-universe models to quantify whether they fit the data by employing a statistic that searches for topology-induced symmetries in the CMB sky [19]. In Section III B, we search for matched circles in the CMB sky, an idea proposed by [29], ruling out the simplest class of small-universe models. Finally, we present our conclusions in Section IV.

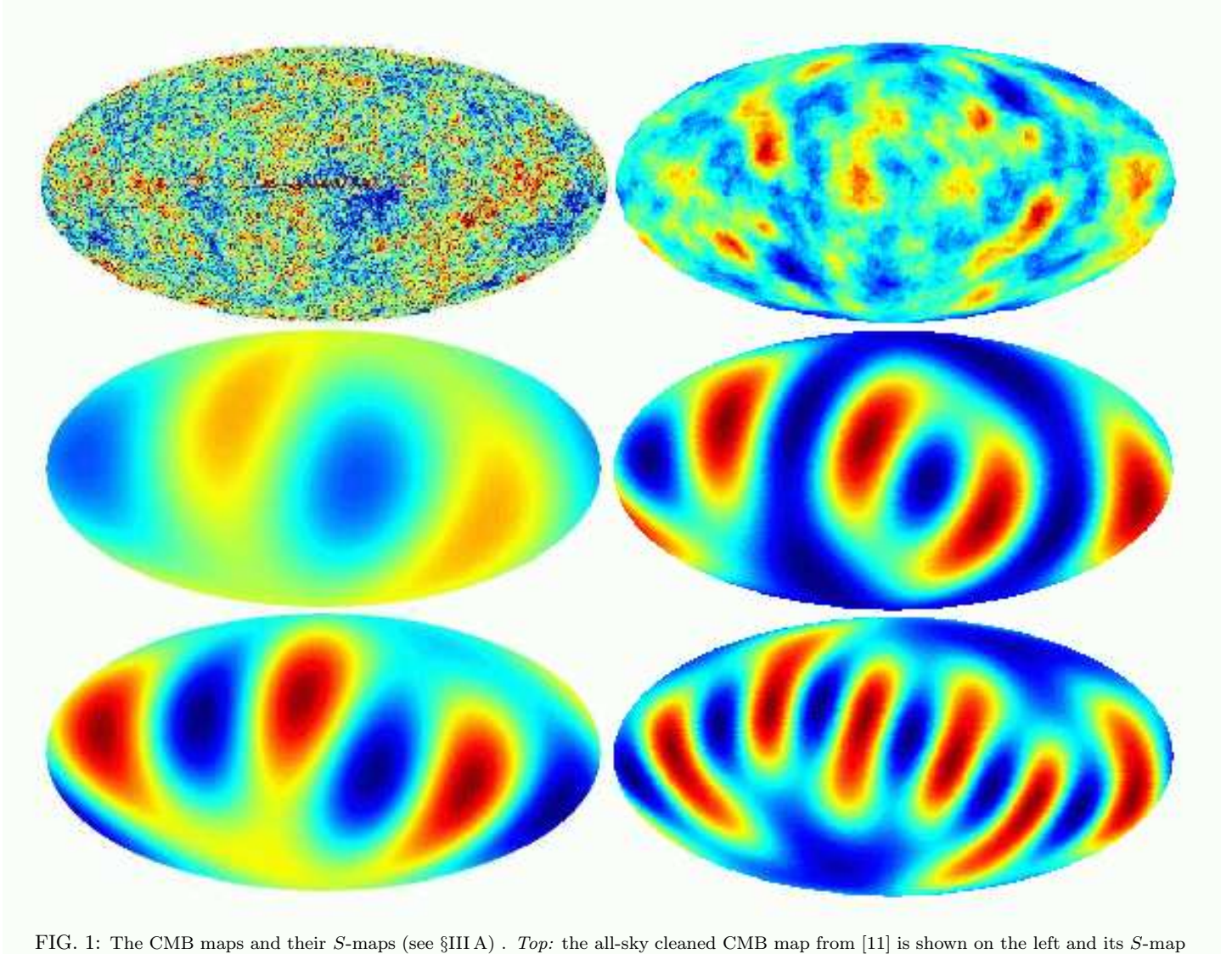


FIG. 1: The CMB maps and their  $S$ -maps (see §III A) . *Top*: the all-sky cleaned CMB map from [11] is shown on the left and its  $S$ -map on the right. *Middle*: the quadrupole map (left) and its  $S$ -map (right). *Bottom*: the octopole map (left) and its  $S$ -map (right). Note that all three  $S$ -maps show dark spots in the supposed direction of suppression of its original maps, around “two o’clock”.

TABLE I: CMB quadrupole and octopole power.

Measurement	$\delta T_2^2$ [ $\mu\text{K}^2$ ]	p-value	$\delta T_3^2$ [ $\mu\text{K}^2$ ]
Spergel <i>et al.</i> model	869.7		855.6
Hinshaw <i>et al.</i> cut sky	123.4	0.7%	611.8
ILC map all sky	195.1	4.8%	1053.4
Tegmark <i>et al.</i>	201.6	5.1%	866.1
Cosmic quadrupole	194.2	4.7%	
Dynamic quadrupole	3.6		

## II. HOW SIGNIFICANT ARE THE “ANOMALIES” IN THE LOWER MULTIPOLES?

### A. The low quadrupole

The surprisingly small CMB quadrupole has intrigued the cosmology community ever since it was first observed by COBE/DMR [8]. However, it was not until the precision measurements of WMAP [10] that it became clear that the anomaly could not be blamed on Galactic foreground contamination. Simulations by [5, 6] have demonstrated that within the context of the standard inflationary  $\Lambda$ CDM concordance model, the low large-scale power observed is sufficiently unlikely to warrant serious concern. The WMAP team argued that the low quadrupole requires a fluke at the one in 143 level and the low overall large-scale power (mainly quadrupole and octopole) require a one in 666 fluke [5].

In [11], it was argued that this deficit of large-scale power was of lower statistical significance than previously claimed, and this conclusion has been strengthened by [7, 12]. In particular, [7] gives a thorough discussion of this statistical issue in the context of both frequentist and Bayesian analysis, concluding that the WMAP results are in fact consistent with the concordance  $\Lambda$ CDM model. Here, we will further elaborate the foreground-related point raised in [11]. The WMAP team measured the angular power spectrum  $C_\ell$  using only the part of the sky outside of their Galactic cut, and [11] found that this cut, seemingly coincidentally, eliminated the strongest hot/cold spots of the quadrupole and octopole. To correctly interpret the low *a priori* likelihood of the WMAP measurements, we need to factor it as a product of two different probabilities, corresponding to the following two questions:

1. *How unlikely is the all-sky power spectrum given a cosmological model like  $\Lambda$ CDM?*
2. *Given the all-sky CMB map, how unlikely is it that the Galactic cut will eliminate such a large fraction of the quadrupole and octopole power?*

The key point is that the location of the Galactic cut is determined by the orientation of the Milky Way, *i.e.*, by fluctuations that have nothing to do with the CMB

TABLE II: Observed CMB quadrupole and octopole coefficients in the foreground-cleaned WMAP map [11] calculated in Galactic coordinates in units of  $\mu\text{K}$ .

$\ell$	$m$	$\text{Re}\{a_{\ell m}\}$	$\text{Im}\{a_{\ell m}\}$
2	0	10.73	0.00
2	1	-5.87	4.26
2	2	-13.71	-15.15
3	0	-6.52	0.00
3	1	-9.08	0.68
3	2	21.57	1.73
3	3	-13.64	28.79

quadrupole and octopole. This means that although an unlikely coincidence associated with the second question may be disturbing, it is of no cosmological significance and should be ignored when testing cosmological models.

Table I summarizes measurements of the quadrupole (column 2) and octopole (column 4) power reported in [2, 5, 11]. Table II gives a breakdown of the coefficients  $a_{\ell m}$  which produce the quadrupole and octopole power given in row 4 of Table I, according to

$$\delta T_\ell^2 = \ell(\ell + 1)C_\ell/2\pi,$$

with

$$C_\ell = (2\ell + 1)^{-1} \sum_{\ell=-m}^m |a_{\ell m}|^2.$$

The third column of Table I shows the probability of the quadrupole in our Hubble volume being as low as observed if the best-fit WMAP team model from [5, 6] is correct. For the all-sky case where  $\delta T_2^2$  has a  $\chi^2$ -distribution with 5 degrees of freedom, the probability tabulated is simply

$$1 - \gamma[5/2, (5/2)T_2^2/855.6\mu\text{K}^2]/\Gamma(5/2),$$

where  $\gamma$  and  $\Gamma$  are the incomplete and complete Gamma functions, respectively. According to Question 1, the low cosmic quadrupole requires about a one in 20 coincidence, and the cosmic octopole is not low at all, actually exceeding the theoretical prediction. The one in 666 coincidence from [5] thus factors roughly into a one in 20 cosmic coincidence (Question 1) and a one in 33 Galactic orientation coincidence (Question 2).

Foreground modeling remains the dominant uncertainty underlying these arguments. Although the detailed tests reported in [11] suggested that the quadrupole and octopole contributions from the inner Galactic plane were unimportant (after multifrequency

foreground subtraction), this issue deserves further study. Moreover, exotic foreground processes that are not localized to the Galactic plane, say SZ-emission from the Galactic halo or the local super-cluster, would not have been detected in these tests. If a substantial fraction of the all-sky power reported in Table II turns out to be attributable to contamination, this will of course exacerbate the problem for the  $\Lambda$ CDMs cosmological model.

### B. The quadrupole-octopole alignment

As seen in Figure 1, the quadrupole of the foreground-cleaned WMAP map [11] (at middle left in the figure) and octopole (at bottom left) both appear rather planar, with most of their hot and cold spots centered on a single plane in the sky<sup>1</sup>. Moreover, the two planes appear roughly aligned. *Can we quantify the statistical significance of this alignment?*

A simple way to quantify a preferred axis for arbitrary multipoles is to think of the CMB map as a wave function

$$\frac{\delta T}{T}(\hat{\mathbf{n}}) \equiv \psi(\hat{\mathbf{n}})$$

and find the axis  $\hat{\mathbf{n}}$  around which the angular momentum dispersion

$$\langle \psi | (\hat{\mathbf{n}} \cdot \mathbf{L})^2 | \psi \rangle = \sum_m m^2 |a_{\ell m}(\hat{\mathbf{n}})|^2 \quad (1)$$

is maximized. Here  $a_{\ell m}(\hat{\mathbf{n}})$  denotes the spherical harmonic coefficients of the CMB map in a rotated coordinate system with its  $z$ -axis in the the  $\hat{\mathbf{n}}$ -direction. In practice, we perform the maximization by evaluating equation (1) at all the unit vectors  $\hat{\mathbf{n}}$  corresponding to 3,145,728 HEALPix<sup>2</sup> pixel centers at resolution  $n_{\text{side}}=512$ , which pinpoints the maximum to within half the pixel spacing, about 0.06 degrees. Table II lists the coefficients  $a_{\ell m}$  for  $\ell = 2, 3$  in Galactic coordinates. We then use Wigner's formula (see Appendix A) to rotate these coefficients into other coordinate systems, which is much faster than repeatedly rotating the entire sky map. We find the preferred axes  $\hat{\mathbf{n}}_2$  and  $\hat{\mathbf{n}}_3$  for the quadrupole and octopole, respectively, to be

$$\begin{aligned} \hat{\mathbf{n}}_2 &= (-0.1145, -0.5265, 0.8424), \\ \hat{\mathbf{n}}_3 &= (-0.2578, -0.4207, 0.8698), \end{aligned} \quad (2)$$

*i.e.*, both roughly in the direction of  $(l, b) \sim (-110^\circ, 60^\circ)$  in Virgo.

TABLE III: Real-valued quadrupole and octopole coefficients  $\tilde{a}_{\ell m}$  (defined in Appendix A) in Galactic coordinates (left) and rotated into their preferred frame of equation (2) (right), in units of  $\mu\text{K}$ . The observed  $\delta T_\ell$  for  $\ell = 2, 3$  are the rms of these numbers times  $[\ell(\ell+1)/(2\pi)]^{1/2}$ .

$\ell$	$m$	Galactic	Rotated
2	-2	-21.43	13.32
2	-1	6.03	-0.40
2	0	10.73	6.72
2	1	-8.30	-0.40
2	2	-19.39	28.86
3	-3	40.71	50.58
3	-2	2.45	-1.67
3	-1	0.96	-0.50
3	0	-6.52	-13.60
3	1	-12.84	-0.27
3	2	30.50	0.71
3	3	-19.29	-20.68

Under the null hypothesis that the CMB is an isotropic random field, the quadrupole and octopole are statistically independent, with the unit vectors  $\hat{\mathbf{n}}_2$  and  $\hat{\mathbf{n}}_3$  being independently drawn from a distribution where all directions are equally likely. This means that the dot product  $\hat{\mathbf{n}}_2 \cdot \hat{\mathbf{n}}_3$  is a uniformly distributed random variable on the interval  $[-1, 1]$ <sup>3</sup>. Equation (1) does not distinguish between  $\hat{\mathbf{n}}$  and  $-\hat{\mathbf{n}}$  (we find a preferred axis, not a preferred direction), so let us quantify the alignment by studying the quantity  $|\hat{\mathbf{n}}_2 \cdot \hat{\mathbf{n}}_3|$  which has a uniform distribution on the unit interval  $[0, 1]$ . Equation (2) gives  $|\hat{\mathbf{n}}_2 \cdot \hat{\mathbf{n}}_3| \approx 0.9838$ , corresponding to a separation of  $10.3^\circ$ . An alignment this good happens by chance only once in  $1/(1 - 0.9838) \approx 62$ . In other words, the probability that a random axis falls inside a circle of radius  $10.3^\circ$  around the quadrupole axis is simply the area of this circle over the area of the half-sphere,  $1/62$ .

Although [11] argued that residual foreground contamination is not likely to dominate the quadrupole or octopole, it is important to keep in mind the possibility that some form of residual foreground contamination might nonetheless contribute to the alignment of the two. Note that the plane orthogonal to the preferred axes given by equation (2) is about  $\cos^{-1} 0.85 \approx 30^\circ$  away from the Galactic plane, which is not particularly significant (requiring only a 1 in 6 coincidence).

<sup>1</sup> Note that this is planarity is somewhat obscured by the Aitoff projection.

<sup>2</sup> The HEALPix package is available from <http://www.eso.org/science/healpix/>.

<sup>3</sup> This is most easily seen as follows. In a coordinate system where  $\hat{\mathbf{n}}_2 = (0, 0, 1)$  and  $\hat{\mathbf{n}}_3 = (\sin \theta \cos \varphi, \sin \theta \sin \varphi, \cos \theta)$ , the dot product is  $\hat{\mathbf{n}}_2 \cdot \hat{\mathbf{n}}_3 = \cos \theta$  which has a uniform distribution, since the area element  $d\Omega = \sin \theta d\theta d\varphi \propto d \cos \theta = d(\hat{\mathbf{n}}_2 \cdot \hat{\mathbf{n}}_3)$ .

### C. The planar octopole

We just discussed the statistical significance of two anomalies: an intrinsic property of the quadrupole (being low) and the alignment between the quadrupole and octopole. Figure 1, however, suggests the presence of a third anomaly intrinsic to the octopole: being unusually planar. In contrast, the hexadecapole and higher multipoles seem to exhibit a more generic behavior, as we expect in an isotropic random field, with no obvious preferred axis. *How unlikely is for an octopole to be so planar by chance?*

According to the first statistical test we performed, using the symmetry statistic that we will describe in detail in the next section, this requires a one in 20 coincidence in the context of a Gaussian random field. Another obvious test involves the angular momentum used in equation (1). We define a test statistic  $t$  that measures the maximal percentage of the octopole power that can be attributed to  $|m| = 3$ , *i.e.*,

$$t \equiv \max_{\hat{\mathbf{n}}} \frac{|a_{3-3}(\hat{\mathbf{n}})|^2 + |a_{33}(\hat{\mathbf{n}})|^2}{\sum_{m=-3}^3 |a_{3m}(\hat{\mathbf{n}})|^2}, \quad (3)$$

and find that for the cleaned WMAP map [11]  $t=94\%$ . Performing a large number of Monte Carlo simulations corresponding to an isotropic Gaussian random field (where the seven real-valued coefficients  $\tilde{a}_{3m}$  are simply independent Gaussian random variables with zero mean and identical variance), we obtain values larger than this about 7% of the time. Redefining  $t$  as the ratio of the angular momentum dispersion to the total power, *i.e.*,  $t \equiv \langle \psi | (\hat{\mathbf{n}} \cdot \mathbf{L})^2 | \psi \rangle / \langle \psi | \psi \rangle$ , gives a similar significance level. In both of these tests, the planar nature of the octopole is reflected by the dominant contribution from  $|m| = 3$  to the octopole rms in the last column of Table III. In contrast, the quadrupole is not significantly planar according to these same statistical tests.

## III. TOPOLOGICAL SIGNATURES

In the previous section, we investigated the anomalies reported in the maps from the WMAP satellite on very large angular scales. Although the *a priori* chance of all these three anomalies occurring is 1 in 24000, the multitude of alternative anomalies one could have looked for dilutes the significance of such *a posteriori* statistics. It is important to point out, however, that in the simplest small Universe model where the Universe has toroidal topology with one small dimension smaller than the horizon scale, one would expect all three of the anomalies discussed above. This means that in the context of constraining cosmic topology, these three effects are not merely three arbitrary ones among many.

Two completely separate observable signatures of small universes have been described in the literature. The first,

known as the  $S$ -statistic [19, 30], assumes that modifications of the CMB power spectrum are caused by the fact that only certain fluctuation modes are allowed by the boundary conditions, just as the fundamental tone and its overtones give information about the geometry inside a flute. The second, known as circles-in-the-sky [29], is a purely geometric effect in which a given space-time point may be observable by us in more than one direction.

These two signatures are both independent and complementary. The information about the first comes from the largest angular scales in the CMB, while information about the second comes from smaller-scale CMB patterns, as well as distant objects such as quasars that could potentially be multiply imaged (see, *e.g.*, [31, 32]). Detection of a signature of the second kind could provide smoking gun evidence of a small universe, being independent of any assumptions about cosmological perturbation theory and potentially providing high statistical significance.

### A. Searching for symmetries in the sky

In this subsection, we investigate whether the WMAP data exhibits the type of large-scale symmetries predicted by small-universe models [19, 30].

#### 1. The $S$ -Statistic

We perform our tests by computing the function  $S(\hat{\mathbf{n}}_i)$  defined by [19, 30]:

$$S(\hat{\mathbf{n}}_i) \equiv \frac{1}{N_{pix}} \sum_{j=1}^{N_{pix}} \left[ \frac{\delta T}{T}(\hat{\mathbf{n}}_j) - \frac{\delta T}{T}(\hat{\mathbf{n}}_{ij}) \right]^2, \quad (4)$$

where  $N_{pix}$  is the number of pixels in the cleaned map and  $\hat{\mathbf{n}}_{ij}$  denotes the reflection of  $\hat{\mathbf{n}}_j$  in the plane whose normal is  $\hat{\mathbf{n}}_i$ , *i.e.*,

$$\hat{\mathbf{n}}_{ij} = \hat{\mathbf{n}}_j - 2(\hat{\mathbf{n}}_i \cdot \hat{\mathbf{n}}_j)\hat{\mathbf{n}}_i. \quad (5)$$

$S(\hat{\mathbf{n}})$  is a measure of how much reflection symmetry there is in the mirror plane perpendicular to  $\hat{\mathbf{n}}$ . The more perfect the symmetry is, the smaller  $S(\hat{\mathbf{n}})$  will be.

We refer to the map of  $S(\hat{\mathbf{n}}_i)$  over the whole sky as an  $S$ -map. This map is a useful visualization tool and gives intuitive understanding of how the  $S$ -statistic works.  $S$ -maps are discussed in more detail in Section III A 2.

For a given sky map, we compute a test statistic  $S_o$  defined as the minimum value of the  $S$ -map. As explained and illustrated in [19], small-universe models with toroidal topology exhibit symmetries that give them on average smaller values of  $S_o$  than infinite universes, which makes the  $S$ -statistic useful for constraining the cosmic topology.

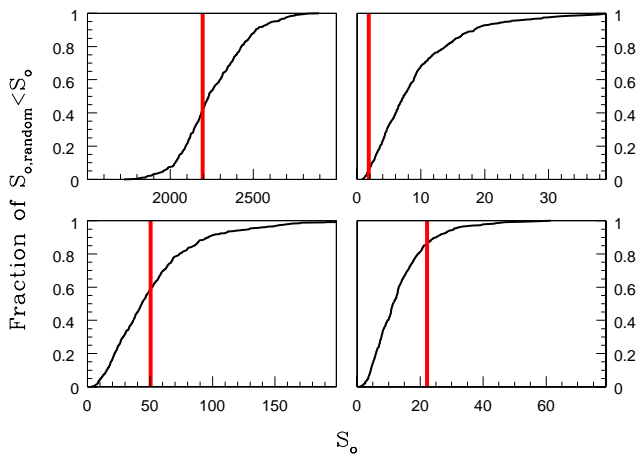


FIG. 2: Cumulative histograms of  $S_0$ . *Top-left*:  $S$ -test for the cleaned WMAP map. *Top-right*:  $S$ -test for octopole alone. *Bottom-left*:  $S$ -test for the sum of the quadrupole and octopole. *Bottom-right*:  $S$ -test for hexadecapole alone. Curves show the fraction of 500 simulated maps that have  $S_0$  below the given value. A small Universe should give a small  $S_0$ -value, but the observed value of  $S_0^{WMAP}$  (vertical line) is seen to be significantly smaller than expected in an infinite universe only for the octopole case.

## 2. $S$ -maps from the WMAP data

The  $S$ -map of our WMAP cleaned map from [11] is shown in Figure 1 (top right), and shows a striking pair of dark spots on the same preferred axis that we identified in Section II B, equation (2), at “two o’clock” and its antipode. Such an isolated minimum in the  $S$ -map is characteristic of a  $T^1$ -model, where the Universe is a 3-torus with only one direction small relative to the cosmic horizon. Figure 1 also shows the  $S$ -maps of the quadrupole (middle right) and the octopole (bottom right) components, and both are seen to independently show dark spots along this special axis. In contrast, the  $S$ -maps of the hexadecapole and higher multipoles do not have this property.

## 3. What is the probability that an infinite Universe possesses such symmetry?

To quantify the statistical significance of this symmetry axis, we produced 500 all-sky Monte Carlo simulations with HEALpix resolution  $n_{side}=16$ , with monopole and dipole removed, adopting  $\ell_{max}=128$ , and using the WMAP  $\Lambda$ CDM fiducial power spectra of [5]. We then use equation (4) to compute the  $S$ -map and  $S_0$  for each of those 500 simulations. Figure 2 (top left) shows a cumulative histogram of  $S_0$  for these 500 simulations. For comparison, the vertical line corresponds to the value of  $S_0^{WMAP}$  for the real WMAP data processed in the same way. The fact that  $S_0^{WMAP}$  for the real data falls near the middle of the distribution means that although the dark spots in seen in Figure 1 (top right) may appear

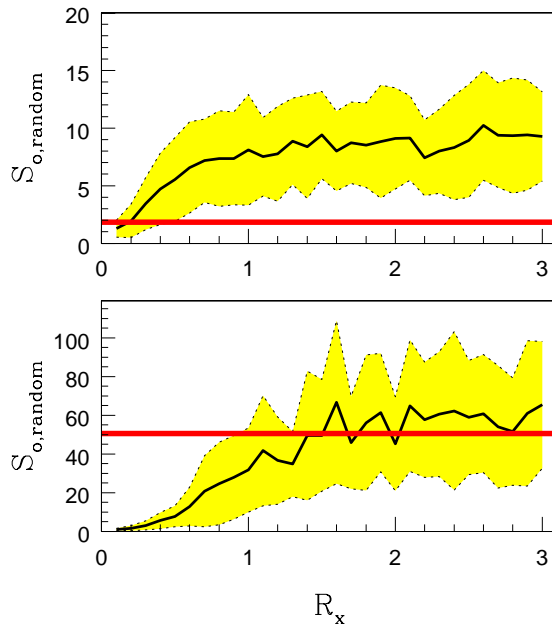


FIG. 3: Expected and observed  $S_0$ -values for the octopole map alone (top) and for the sum of the quadrupole and octopole maps (bottom). The solid line shows the mean of the Monte Carlo simulations and the yellow (or grey in BW) band shows the  $1 - \sigma$  spread. 120 simulations per  $R_x$ -value were performed for  $R_x \leq 1$  and 30 per  $R_x$ -value for  $R_x > 1$ . The horizontal lines represent the observed values  $S_0^{WMAP}$ .

visually striking, symmetries at this level are not at all unlikely to happen by chance in an infinite universe. In other words, the WMAP data is perfectly consistent with a standard infinite universe as far as our  $S$ -test is concerned. We obtain similar results when analyzing the octopole alone (top right), the hexadecapole alone (bottom right), various higher multipoles alone, as well as the sum of quadrupole and octopole (bottom left). For the case of the octopole (top right), however, we find the high degree of symmetry to be marginally significant, with an  $S_0$ -value as low as observed by WMAP occurring in less than 5% of the simulations. If the octopole had all its hot and cold spots centered on a single plane, it would have perfect reflection symmetry about this plane, so this one in 20 anomaly is simply another manifestation of the planar nature of the octopole discussed in Section II C.

Note that there is nothing to be learned from applying the  $S$ -test to multipoles  $\ell = 0, 1$  or  $2$  on their own, since (apart from pixelization effects) they all give  $S_0 = 0$ . The monopole exhibits perfect symmetry around any axis, so its  $S$ -map is identically zero. The dipole has perfect reflection symmetry in all axes perpendicular to the dipole direction, so its  $S$ -map equals zero on a great circle. The quadrupole is a quadratic function given by a symmetric  $3 \times 3$  matrix, and therefore has perfect reflection symmetry about the three orthogonal eigenvectors of this matrix. This is illustrated in Figure 1, where the quadrupole  $S$ -map (middle right) exhibits six zeroes corresponding to the pair of hot spots, the pair of cold spots and the pair

of saddle points in the quadrupole map (middle left).

#### 4. Making Toroidal Fake Skies

Above we found that the  $S$ -statistic was consistent with an infinite universe. Since a small universe could nonetheless explain all three of the anomalies of Section II in one fell swoop, let us investigate whether small universes provide a better fit to the data than an infinite universe does or, conversely, whether the  $S$ -statistic rules out some interesting class of small universe models.

In a toroidal universe, only wave numbers that are harmonics of the cell size are allowed. Therefore, we have a discrete  $\mathbf{k}$  spectrum [33, 34]

$$\mathbf{k} = \frac{2\pi}{R_H} \left( \frac{p_x}{R_x}, \frac{p_y}{R_y}, \frac{p_z}{R_z} \right), \quad (6)$$

where  $p_x, p_y$  and  $p_z$  are integers, and  $R_x, R_y$  and  $R_z$  are the sizes of the cell. It was shown in [19] that toroidal universes can be simulated by

$$\frac{\delta T}{T}(\theta, \phi) \propto \sum_{p_x, p_y, p_z} [g_1 \cos(2\pi\gamma) + g_2 \sin(2\pi\gamma)] \alpha^{\frac{n-4}{4}}, \quad (7)$$

where

$$\gamma = \left( \frac{p_x}{R_x}x + \frac{p_y}{R_y}y + \frac{p_z}{R_z}z \right), \quad (8)$$

$$\alpha \equiv \frac{R_H |\mathbf{k}|}{2\pi} = \left( \frac{p_x}{R_x} \right)^2 + \left( \frac{p_y}{R_y} \right)^2 + \left( \frac{p_z}{R_z} \right)^2, \quad (9)$$

$g_1$  and  $g_2$  are two unit Gaussians random variables, and  $n$  is the spectral index<sup>4</sup>. We generate our simulations with  $n = 1$  since this provides a good fit to the observed CMB power spectrum on the large angular scales that matter here (our tests below use only the information at the lowest multipoles). The symmetry patterns expected in  $T^1$  universes have been shown to appear for broad range of  $n$ -values (actually,  $n < 3$ ) [19]. Since we are focusing on  $T^1$  universes, we wish to set  $R_y = R_z = \infty$ . In practice, we set  $R_y = R_z = 3$ , since this is more numerically convenient and essentially indistinguishable in practice. We add no noise to the simulations, since WMAP detector noise is completely negligible for  $\ell \leq 20$ .

#### 5. If we live in a $T^1$ , can we constrain the cell size $R_x$ ?

For the tests in this section, we create two band-pass filtered versions of the foreground-cleaned WMAP map,

retaining only  $\ell = 3$  and only  $2 \leq \ell \leq 3$ , respectively. We then degrade the resolution of these two maps to HEALpix resolution  $n_{\text{side}}=16$ . After generating our simulated small universe maps as above, we band-pass filter and process them in the same way as the real data. Since we wish to test only for symmetry properties, we normalize the two types of Monte Carlo maps to have the same rms fluctuations as the two corresponding filtered WMAP maps.

Fixing a cell size, we constructed a simulated CMB map as described above and used equation (4) to obtain an  $S$ -map from which we extracted its minimum value  $S_o$ . Repeating this procedure 120 times, we obtain the probability distribution of  $S_o$  for a given cell size. When we repeat this procedure for different cell sizes we are able to construct Figure 3.

In Figure 3, we show the probability distribution of  $S_o$  obtained from Monte Carlo simulations for cell sizes  $0.1 < R_x < 3$ . Comparing this with the horizontal solid line (which represents the  $S_o$ -value extracted from the WMAP data,  $S_o^{WMAP}$ ) shows what range of  $R_x$ -values WMAP favors. The octopole alone (top panel) is seen to favor a small Universe with  $R_x < 0.5$  at the  $1 - \sigma$  level, since it has near reflection symmetry about the preferred plane discussed in Section II C. However, the quadrupole-octopole combination (bottom panel) is seen to disfavor small universes, preferring  $R_x \gtrsim 1$ . We repeated the same test for all individual multipoles  $\ell = 4, \dots, 10$  and for the ranges  $2 - 10$ ,  $11 - 20$  and  $2 - 20$ , finding no significant preference for small universes. Combining the evidence of all these tests, we therefore conclude that the WMAP  $S$ -test does not favor the small universe hypothesis, preferring a cell size at least as large as our Hubble Volume,  $R_x \gtrsim 1$ .

#### B. Searching for circles in the sky

The circles method [29] involves matching circles in the CMB sky. The CMB Surface of Last Scattering (SLS) imaged by WMAP is a sphere with us at its center. The simple case of a toroidal Universe is mathematically equivalent to a perfectly periodic Universe, with copies of us on an infinite rectangular lattice. Since each copy of us is surrounded by its own spherical SLS, and the intersection of two spheres a circle, it follows that if the lattice spacing is smaller than the diameter of the sphere, we can observe the same circular part of the SLS in opposite directions in the sky. In the case of a sufficiently small spacing, there will be several such matched circles, all concentric. As shown in [29], this result is general: *any* compact topology generates matched circles. For more complicated cases, these circles will typically no longer be opposite from one another as mirror images, but can differ in location, size, rotation and parity.

<sup>4</sup> A more realistic Monte Carlo can be done by adding to each toroidal simulation a map that has only the ISW contribution. A power suppression and enhanced symmetry at low multipoles would remain.

### 1. Real-world complications

In the original discussion of this effect, [29] considered the idealized case where the entire CMB signal came from the SLS and would look the same from different vantage points. In practice, however, we need to consider three important departures from these assumptions:

1. The late integrated Sachs-Wolfe (LISW) effect is generated not on the SLS but later on, by the gravitational potential that the CMB photons traverse en route to us, so this contribution to the WMAP map will *not* match between paired circles.
2. Whereas the CMB fluctuations generated by SLS density fluctuations and gravitational potential fluctuations look the same from any vantage point, those generated by the Doppler effect from velocity perturbations do not. Rather, they have a dipole structure, which means that what looks like a hot spot from one vantage point looks like a cold spot when viewed from the opposite direction. The Doppler contribution to CMB fluctuations therefore does not match between paired circles, and will in fact be strongly anti-correlated for small matched circles (whose features we view from nearly opposite directions).
3. The contribution to CMB maps from foreground contamination and detector noise will not match between paired circles.

To minimize the effect described in the third item, we based our analysis on the foreground-cleaned WMAP map from [11], which minimizes the combined fluctuations of foregrounds and noise. Although residual foreground contamination may prevent us from finding a pair of small matched circles hiding in the Galactic plane, the above-mentioned axis that we are most interested in is fortunately nowhere near this plane.

We tackle the effects described in items 1 and 2 by filtering the WMAP map before performing the circle search. Since the LISW effect is important only for the very largest multipoles, we can high-pass filter the WMAP map by zeroing all multipoles with  $\ell < 8$ , therefore removing the contributions from 1. The Doppler effect, on the other hand, is dominant only in the troughs between the acoustic peaks (it is mainly this effect that prevents the CMB power spectrum from dropping all the way down to zero between the peaks). Therefore, we can remove the contributions from 2 by zeroing all multipoles with  $\ell > 300$  as well. If we were to detect a suspected matched circle pair, a powerful subsequent consistency test would be whether an  $\ell = 301 - 400$  band-pass filtered map (probing roughly the first acoustic trough) displays anti-correlation between the two circles.

The issue of how to best deal with the above-mentioned real-world complications for circle matching is an interesting and challenging data analysis problem, worthy of a future paper in its own right. Our analysis here should simply be viewed as a first attack on the problem, and

the forthcoming analysis by [37], in preparation, will undoubtedly improve it. One challenge is that band-pass filtering is spatially non-local, potentially reducing detectability by smearing out matched circles and by superimposing signal from neighboring sky regions on the circles. A second challenge is how to optimally deal with the fact that the WMAP map is pixelized. This means that there generally will not be a pixel centered exactly at the desired reflected position  $\hat{\mathbf{n}}_{ij}$  in equation (10) below — in this paper, we simply use the closest pixel. This pixelization problem is exacerbated by a desire to perform the circle search at as low resolution as possible to avoid the computations becoming prohibitively slow.

### 2. The search

We limit our search to the simplest class of small-universe models, the ones where space is flat and toroidal. For this simple case, the matched circles come in diametrically opposed pairs, specified by three parameters: the position, given by  $(l, b)$  for the center of a circle, and its angular radius  $\alpha$ . A much more ambitious six-parameter search corresponding to the general case will be presented by Spergel *et al.* [37].

To search for matched circles, we define a family of difference maps. For a given axis  $\hat{\mathbf{n}}_i$ , the map is defined through

$$D(\hat{\mathbf{n}}_i) \equiv \frac{\delta T}{T}(\hat{\mathbf{n}}_j) - \frac{\delta T}{T}(\hat{\mathbf{n}}_{ij}), \quad (10)$$

where  $\hat{\mathbf{n}}_{ij}$  denotes the reflection of  $\hat{\mathbf{n}}_j$  in the plane whose normal is  $\hat{\mathbf{n}}_i$  (*i.e.*,  $\hat{\mathbf{n}}_{ij}$  is given by equation (5)). In other words, the map  $D$  is just the original WMAP map minus its reflection about the plane normal to  $\hat{\mathbf{n}}_i$ . Note that equation (10) and equation (4) are closely related:  $S_0$  is simply the smallest average of a squared  $D$ -map. In the ideal case of a perfectly matched circle pair, it would manifest itself as a pair of  $D = 0$  circles in a  $D$ -map that otherwise fluctuates with about twice the variance of the original WMAP map. Note that in addition, there will always be a great ( $\alpha = 90^\circ$ ) circle with  $D = 0$  lying in the reflection plane: here the WMAP map is of course equal to its reflection, so the  $D$ -map will automatically vanish.

To distill out this matched circle information, we replace each  $D$ -map by a single curve  $d(\alpha; \hat{\mathbf{n}}_i)$  giving its rms along circles making a constant angle  $\alpha$  with the reflection axis, *i.e.*, with  $\hat{\mathbf{n}}_i \cdot \hat{\mathbf{n}}_j = \cos \alpha$ . An example of such a curve (for a fixed  $\hat{\mathbf{n}}_i$ ) is shown in Figure 4. In practice, the HEALpix pixelization subdivides the sky into  $12n^2$  pixels, where the  $n$  is a power of two determining the resolution. We compute  $d(\alpha)$  in  $n$  angular bins equispaced in  $\cos \alpha$ , which corresponds to a bin width about 0.87 times the pixel side  $(4\pi/12)^{1/2}/n$  for  $\alpha = 30^\circ$ . The advantage of this binning scheme is that each bin gets contributions from about the same number of pixels,  $12n$ . We

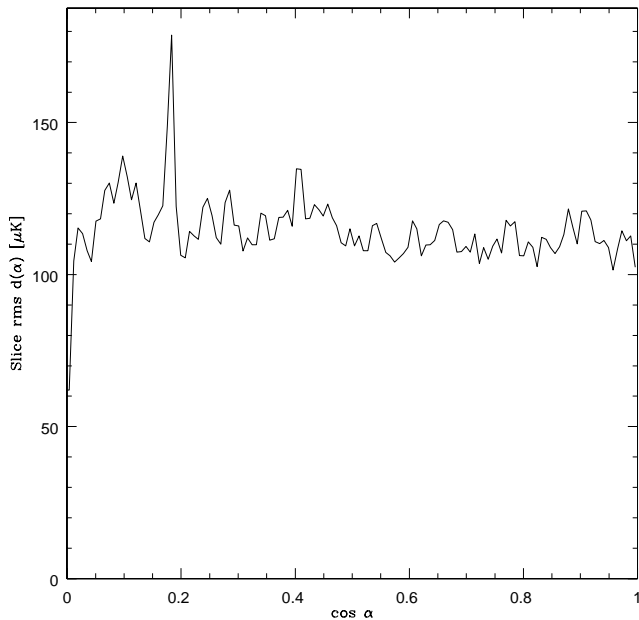


FIG. 4: An example of the curve  $d(\alpha; \hat{\mathbf{n}}_i)$  that we used to search for matched circles. This case is for the reflection axis  $\hat{\mathbf{n}}_i$  corresponding to  $(l, b) = (-110^\circ, 60^\circ)$ . A pair of perfectly matched circles of angular radius  $\alpha$  would give  $d(\alpha) = 0$ . The drop towards zero on the left hand side is caused by a great ( $\alpha = 90^\circ$ ) circle being its own reflection, whereas the high values around  $\alpha \sim 15^\circ$  are caused by residual foreground contamination.

performed our analysis with  $n = 256$ , which took a couple of weeks on a 2 GHz linux workstation. For a given potential circle center  $\hat{\mathbf{n}}_i$ , the curve  $d(\alpha; \hat{\mathbf{n}}_i)$  will thus oscillate randomly as a function of  $\alpha$  with roughly constant variance, as shown in Figure 4. Apart from pixelization effects, this curve will drop to zero at any  $\alpha$  corresponding to a perfectly matched circle. Figure 4 shows such a deep minimum only for  $\alpha = 90^\circ$ , the above-mentioned case of the  $90^\circ$  circle which of course equals its own reflection.

To analyze the results of our search, we compute a summary map  $d_{\min}$ , defined as

$$d_{\min}(\hat{\mathbf{n}}_i) \equiv \min_{\alpha_0 < \alpha < \alpha_1} d(\alpha; \hat{\mathbf{n}}_i). \quad (11)$$

If matched circles are present, the summary map should show evidence for these circles in the radius range from  $\alpha_0$  to  $\alpha_1$ , and each pixel in this map should correspond to the evidence for circles centered on that pixel.

Figure 5 shows the summary map for circle radii in the range  $0^\circ < \alpha < 15^\circ$ . The color scale is seen to range over about a factor of two in  $d$ -value (the units are  $\mu\text{K}$ ). A matched circle would correspond to a pair of diametrically opposite pixels with values near zero. Not only are no such pixels seen, but the map shows that the region around  $(l, b) = (-110^\circ, 60^\circ)$  that we are particularly interested in given the quadrupole-octopole anomalies is in no way unusual compared to the rest of the map. The larger values seen near the equator of the

map are caused by residual foreground contamination, which from the definition of the  $d_{\min}$  maps propagates about one circle radius from the Galactic plane. Whereas this foreground contamination can mask true matched circles centered in this region, it can clearly never create false positives, since it increases rather than decreases the  $d_{\min}$ -value.

We computed analogous maps for four other ranges of circle sizes  $\alpha$ ,  $15^\circ - 30^\circ$ ,  $30^\circ - 45^\circ$ ,  $45^\circ - 65^\circ$ ,  $65^\circ - 85^\circ$ , again finding no evidence of matched circles. For completeness, we also computed a final map for the  $\alpha$ -range  $85^\circ - 90^\circ$  obtaining roughly zero, since all  $90^\circ$  circles are matched with themselves.

In conclusion, we find no evidence for the matched circles that are predicted for a simple toroidal universe.

#### IV. CONCLUSIONS

We have investigated anomalies reported in the Cosmic Microwave Background maps from the WMAP satellite on very large angular scales. There are three independent anomalies involving the quadrupole and octopole:

1. The cosmic quadrupole on its own is anomalous at the 1-in-20 level by being low (the cut-sky quadrupole measured by the WMAP team is more strikingly low, apparently due to a coincidence in the orientation of our Galaxy of no cosmological significance).
2. The cosmic octopole on its own is anomalous at the 1-in-20 level by being very planar.
3. The alignment between the quadrupole and octopole is anomalous at the 1-in-60 level.

Although the *a priori* chance of all three occurring is 1 in 24000, the multitude of alternative anomalies one could have looked for dilutes the significance of such *a posteriori* statistics.

However, in the context of constraining cosmic topology, these three effects are not merely three arbitrary ones among many. Indeed, the simplest small Universe model where the Universe has toroidal topology with one small dimension of order half the horizon scale, in the direction towards Virgo, could explain 1, 2 and 3. In order to test this hypothesis, we applied the  $S$ -statistic and the circle test on the WMAP data, ruling out this model. In other words, we have ruled out the “plain bagel” small universe model.

Our results also rule out other models that predict back-to-back matched circles. However, they do not rule out the recently proposed dodecahedron model of [35]: although this model predicts six pairs of diametrically opposed circles of radius about  $35^\circ$ , the circles have a  $36^\circ$  twist relative to their twin images, thereby eluding our search method. After the original version of this paper had been submitted, a more thorough analysis by Cornish and collaborators [36] confirmed our findings and

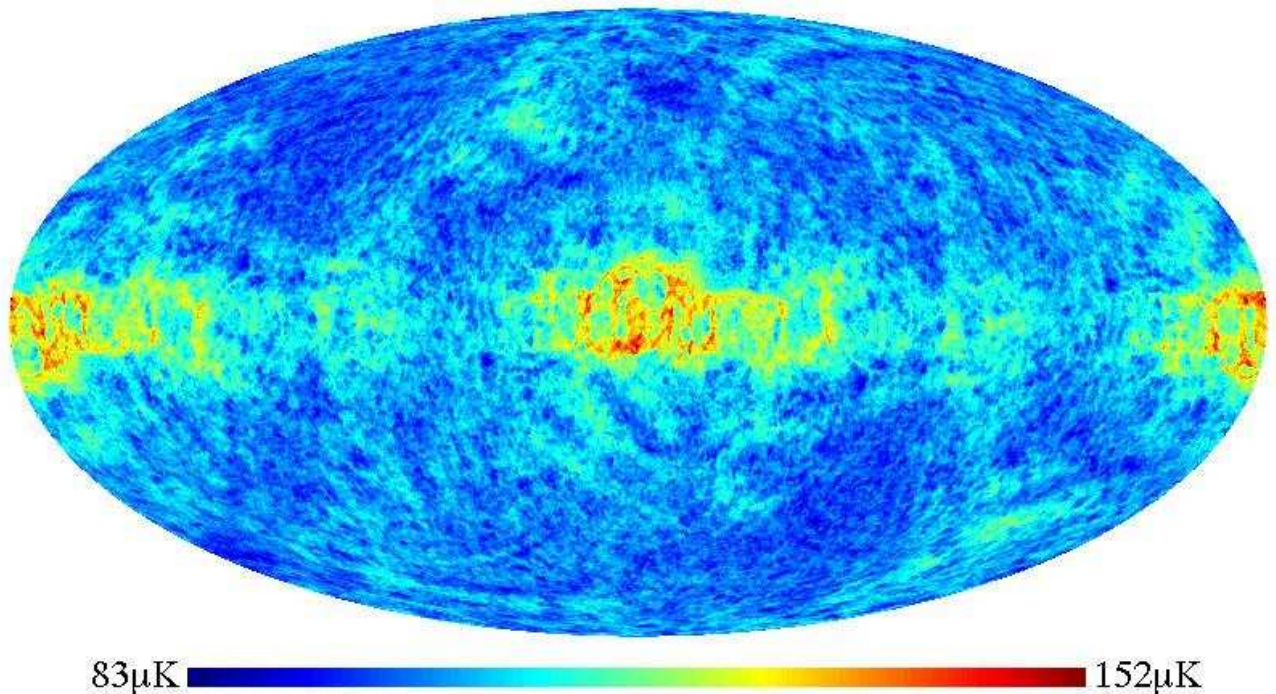


FIG. 5: Result of search for matched circles of radius  $0^\circ < \alpha < 15^\circ$ . A perfectly matched circle would show up as a pixel with zero temperature at the position of the circle center, whereas the map above shows no pixels below  $83\mu\text{K}$ . Note that this map is parity-symmetric, *i.e.*, the temperature at  $\hat{\mathbf{n}}$  equals that at  $-\hat{\mathbf{n}}$ , although this symmetry is obscured by the Aitoff projection used.

improved them to rule out this and other twisted back-to-back models as well.

A maximally ambitious six-parameter “everything bagel” circle search, corresponding to the general case of arbitrary topologies, is currently being carried out by Spergel and collaborators, and will be presented in a forthcoming paper [37]. This should provide decisive evidence either for or against the small universe hypothesis. If this circle search confirms our finding that small universes cannot explain the anomalies, we will be forced to either dismiss the anomalies as a statistical fluke or to search for explanations elsewhere, such as modified inflation models [21–26]. Even the fluke hypothesis might ultimately be testable, since it may be possible to improve the signal-to-noise of the large scale power spectrum beyond the WMAP cosmic variance limit by employing cluster polarization [38, 39] or weak gravitational lensing [40] techniques.

We thank the the WMAP team for producing such a superb data set and for promptly making it public via the Legacy Archive for Microwave Background Data Analysis (LAMBDA) – the WMAP data are available from <http://lambda.gsfc.nasa.gov>. Support for LAMBDA is provided by the NASA Office of Space Science. We thank Krzysztof Górski and collaborators for creating the HEALPix package [41, 42], which we used both for harmonic transforms and map plotting. Thanks to James Bjorken for stimulating discussions. This work was supported by NASA grant NAG5-11099. MT is supported by NSF grant AST-0205981 and a Cottrell Scholarship from Research Corporation. MT & MZ are supported by David and Lucile Packard Foundation fellowships. MZ is supported by NSF and AJSH is supported by NSF grant AST-0205981 and NASA grant NAG5-10763.

- 
- [1] C. L. Bennett *et al.*, astro-ph/0302207 (2003).
  - [2] G. Hinshaw *et al.*, astro-ph/0302217 (2003).
  - [3] X. Wang, M. Tegmark, and M. Zaldarriaga, astro-ph/0105091 (2001).
  - [4] G. Efstathiou *et al.*, astro-ph/0109152 (2001).
  - [5] D. N. Spergel *et al.*, astro-ph/0302209 (2003).
  - [6] L. Verde *et al.*, astro-ph/0302218 (2003).
  - [7] G. Efstathiou *et al.*, astro-ph/0306431 (2003).
  - [8] G. F. Smoot *et al.*, ApJ **396**, 1 (1992).
  - [9] G. Hinshaw *et al.*, astro-ph/9601060 (1996).
  - [10] C. L. Bennett *et al.*, astro-ph/0302208 (2003).
  - [11] M. Tegmark, A. de Oliveira-Costa, and A. Hamilton, astro-ph/0302496 (2003).
  - [12] E. Gaztañaga, J. Wagg, T. Multamaki, A. Montaña, and D. H. Hughes, astro-ph/0304178 (2003).
  - [13] I. Y. Sokolov, JETP Lett. **57**, 617 (1993).
  - [14] L. Z. Fang, Mod. Phys. Lett. A **8**, 2615 (1993).
  - [15] D. Stevens, D. Scott, and J. Silk, Phys. Rev. Lett. **71**, 20

- (1993).
- [16] A. de Oliveira-Costa, and G. F. Smoot, *ApJ* **448**, 447 (1995).
  - [17] G. Rocha *et al.*, astro-ph/0205155 (2002).
  - [18] J. Levin, astro-ph/0108043 (2001).
  - [19] A. de Oliveira-Costa, G. F. Smoot, and A. A. Starobinski, *ApJ* **468**, 457 (1996).
  - [20] J. P. Uzan *et al.*, astro-ph/0303580 (2003).
  - [21] G. Efstathiou, astro-ph/0303623 (2003).
  - [22] S. L. Bridle *et al.*, astro-ph/0302306 (2003).
  - [23] J. P. Uzan *et al.*, astro-ph/0302597 (2003).
  - [24] C. R. Contaldi *et al.*, astro-ph/0303636 (2003).
  - [25] J. M. Cline, P. Crotty, and J. Lesgourgues, astro-ph/0304558 (2003).
  - [26] B. Feng, and X. Zhang, astro-ph/0305020 (2003).
  - [27] M. Bastero-Gil, K. Freese, and L. Mersini-Houghton, hep-ph/0306289 (2003).
  - [28] S. DeDeo, R. R. Caldwell, and P. J. Steinhardt, astro-ph/0301284 (2003).
  - [29] N. Cornish, D. Spergel, and G. Starkman, astro-ph/9801212 (1998).
  - [30] A. A. Starobinsky, *JETP Lett.* **57**, 622 (1993).
  - [31] H. V. Fagundes, and U. F. Wichoski, *ApJ* **322**, L5 (1987).
  - [32] S. J. Weatherley *et al.*, astro-ph/0304290 (2003).
  - [33] Y. B. Zel'dovich, *Comm. Astrophys. Space Sci.* **5(6)**, 169 (1973).
  - [34] L. Z. Fang, and M. Houjun., *Mod. Phys. Lett. A* **2**, 229 (1987).
  - [35] J. P. Luminet, J. R. Weeks, A. Riazuelo, R. Lehoucq, and J. P. Uzan, *Nature* **425**, 593 (2003).
  - [36] N. J. Cornish, D. N. Spergel, G. D. Starkman, and E. Komatsu, astro-ph/0310233 (2003).
  - [37] D. Spergel *et al.*, in preparation (2003).
  - [38] M. Kamionkowski, and A. Loeb, *PRD* **56**, 4511 (1997).
  - [39] N. Seto, and M. Sasaki, astro-ph/0009222 (2000).
  - [40] M. Kesden, M. Kamionkowski, and A. Cooray, (2003). astro-ph/0306597
  - [41] K. M. Górski, E. Hivon, and B. D. Wandelt, (1998). astro-ph/9812350
  - [42] K. M. Górski, B. D. Wandelt, Hansen F K, and A. Banday J, astro-ph/9905275 (1999).
  - [43] A. R. Edmonds, *Angular Momentum in Quantum Mechanics* (1957, Princeton Landmarks in Physics, 1996 edition).
  - [44] A. J. S Hamilton, *ApJ* **417**, 19 (1993).
  - [45] T. Risbo, *J. Geodesy* **70**, 383 (1996).

## APPENDIX A: ROTATION

In this appendix, we review the rotation properties of spherical harmonics that were used in Section II B and Section II C. This material is well-known. However, since we found it rather time-consuming to assemble these explicit results from the literature (which contains a variety of notational conventions and is mainly geared towards the general quantum case where functions are complex rather than real), we summarize the results here for the benefit of the reader interested in performing similar calculations. Fortran77 software implementing this is available from the authors upon request.

### 1. Real-valued spherical harmonics

When a function  $\psi(\hat{\mathbf{n}})$  is real-valued, the corresponding spherical harmonic coefficients obey  $a_{\ell-m} = (-1)^m a_{\ell m}^*$ . The need to work with complex numbers is conveniently eliminated by working with real-valued spherical harmonics, which are obtained from the standard spherical harmonics by replacing  $e^{im\phi}$  in their definition by  $\sqrt{2} \sin m\phi$ , 1,  $\sqrt{2} \cos m\phi$  for  $m < 0$ ,  $m = 0$ ,  $m > 0$ , respectively. In other words, the vector of  $2\ell + 1$  complex numbers  $a_{\ell m}$  ( $m = -\ell, \dots, \ell$ ) specifying the  $\ell^{\text{th}}$  harmonic is replaced by a vector of  $2\ell + 1$  real numbers  $\tilde{a}_{\ell m}$  given by  $\sqrt{2} \text{Im } a_{\ell m}$ ,  $a_{\ell 0}$ ,  $\sqrt{2} \text{Re } a_{\ell m}$ . This mapping from  $a_{\ell m}$  to  $\tilde{a}_{\ell m}$  corresponds to multiplication by a unitary matrix  $\mathbf{U}$ ; for example, the  $\ell = 3$  case corresponds to

$$\mathbf{U} = \begin{pmatrix} \frac{-i}{\sqrt{2}} & 0 & 0 & 0 & 0 & \frac{-i}{\sqrt{2}} \\ 0 & \frac{i}{\sqrt{2}} & 0 & 0 & 0 & \frac{-i}{\sqrt{2}} \\ 0 & 0 & \frac{-i}{\sqrt{2}} & 0 & \frac{-i}{\sqrt{2}} & 0 \\ 0 & 0 & 0 & 1 & 0 & 0 \\ 0 & 0 & -\frac{1}{\sqrt{2}} & 0 & \frac{1}{\sqrt{2}} & 0 \\ 0 & \frac{1}{\sqrt{2}} & 0 & 0 & 0 & \frac{1}{\sqrt{2}} \\ -\frac{1}{\sqrt{2}} & 0 & 0 & 0 & 0 & \frac{1}{\sqrt{2}} \end{pmatrix}. \quad (\text{A1})$$

By unitarity,  $\sum_{\ell} |a_{\ell m}|^2 = \sum_{\ell} \tilde{a}_{\ell m}^2$ , and it follows that the desired right-hand-side of equation (1) is simply  $\sum_{\ell} m^2 \tilde{a}_{\ell m}^2$ . The real-valued spherical harmonic coefficients  $\tilde{a}_{\ell m}$  observed by WMAP are listed in Table III for  $\ell = 2, 3$ .

### 2. Rotations

An arbitrary three-dimensional rotation is specified by three Euler angles  $(\phi, \theta, \alpha)$ , defining a rotation by  $\alpha$  around the  $z$ -axis followed by a rotation by  $\theta$  around the  $y$ -axis followed by a rotation by  $\phi$  around the  $z$ -axis. The  $z$ -rotation by  $\phi$  has a trivial effect on the spherical harmonic coefficients, simply multiplying  $a_{\ell m}$  by a phase factor  $e^{im\phi}$ , so the Euler angle  $\phi$  will not affect the absolute value  $|a_{\ell m}|$  and hence the quantity

computed in equation (1). The axis  $\hat{\mathbf{n}}$  mentioned in Section II B thus does not involve  $\phi$  and is defined by  $\hat{\mathbf{n}} = (\sin \theta \cos \alpha, \sin \theta \sin \alpha, \cos \theta)$ . The  $y$ -rotation multiplies the vector of  $(2\ell + 1)$   $a_{\ell m}$ -coefficients for the  $\ell^{\text{th}}$  multipole by the Wigner matrix  $\mathbf{D}^{\ell}(\theta)$  given by [43–45]

$$\mathbf{D}^{\ell}_{mm'}(\theta) = \sum_{k=\max\{0, m+n\}}^{\min\{\ell+m, \ell+n\}} \left(\cos \frac{\theta}{2}\right)^{2k-m-n} \left(\sin \frac{\theta}{2}\right)^{2\ell+m+n-2k} \times (-1)^{k+\ell+m} \frac{\sqrt{(\ell+m)!(\ell-m)!(\ell+n)!(\ell-n)!}}{k!(\ell+m-k)!(\ell+n-k)!(k-m-n)!}. \quad (\text{A2})$$

Transforming to our real-valued spherical harmonic basis, this corresponds to the rotation matrix  $\mathbf{R}_y(\theta) \equiv \mathbf{U}\mathbf{D}^{\ell}(\theta)\mathbf{U}^{\dagger}$  given by

$$\mathbf{R}_y(\theta) = \begin{pmatrix} \cos \theta & -\sin \theta & 0 & 0 & 0 \\ \sin \theta & \cos \theta & 0 & 0 & 0 \\ 0 & 0 & \frac{1+3 \cos 2\theta}{4} & \frac{\sqrt{3}}{2} \sin 2\theta & \frac{1-\cos 2\theta}{4\sqrt{3}} \\ 0 & 0 & \frac{-\sqrt{3} \sin 2\theta}{2} & \cos 2\theta & \frac{\sin 2\theta}{2} \\ 0 & 0 & \frac{1-\cos 2\theta}{4\sqrt{3}} & \frac{-\sin 2\theta}{2} & \frac{3+\cos 2\theta}{4} \end{pmatrix} \quad (\text{A3})$$

for the quadrupole case, and the corresponding matrix for rotations around the  $z$ -axis is

$$\mathbf{R}_z(\varphi) = \begin{pmatrix} \cos 2\varphi & 0 & 0 & 0 & \sin 2\varphi \\ 0 & \cos \varphi & 0 & \sin \varphi & 0 \\ 0 & 0 & 1 & 0 & 0 \\ 0 & -\sin \varphi & 0 & \cos \varphi & 0 \\ -\sin 2\varphi & 0 & 0 & 0 & \cos 2\varphi \end{pmatrix}. \quad (\text{A4})$$

For the octopole case, equation (A3) is replaced by the block-diagonal matrix

$$\mathbf{R}_y(\theta) = \begin{pmatrix} \mathbf{A} & \mathbf{0} \\ \mathbf{0} & \mathbf{B} \end{pmatrix}, \quad (\text{A5})$$

where

$$\mathbf{A} = \begin{pmatrix} \frac{5+3 \cos 2\theta}{8} & \frac{-\sqrt{\frac{3}{2}} \sin 2\theta}{2} & \frac{1-\cos 2\theta}{8\sqrt{15}} \\ \frac{\sqrt{\frac{3}{2}} \sin 2\theta}{2} & \cos 2\theta & \frac{-\sqrt{\frac{3}{2}} \sin 2\theta}{2} \\ \frac{1-\cos 2\theta}{8\sqrt{15}} & \frac{\sqrt{\frac{3}{2}} \sin 2\theta}{2} & \frac{3+5 \cos 2\theta}{8} \end{pmatrix} \quad (\text{A6})$$

and

$$\mathbf{B} = \begin{pmatrix} \frac{3 \cos \theta + 5 \cos 3\theta}{8} & \frac{\sin \theta + 5 \sin 3\theta}{16\sqrt{6}} & \frac{\cos \theta - \cos 3\theta}{8\sqrt{15}} & \frac{3 \sin \theta - \sin 3\theta}{16\sqrt{10}} \\ \frac{-\sin \theta - 5 \sin 3\theta}{16\sqrt{6}} & \frac{\cos \theta + 15 \cos 3\theta}{16} & \frac{-\sin \theta + 3 \sin 3\theta}{16\sqrt{10}} & \frac{\cos \theta - \cos 3\theta}{16\sqrt{15}} \\ \frac{\cos \theta - \cos 3\theta}{8\sqrt{15}} & \frac{\sin \theta - 3 \sin 3\theta}{16\sqrt{10}} & \frac{5 \cos \theta + 3 \cos 3\theta}{8} & \frac{5 \sin \theta + \sin 3\theta}{16\sqrt{6}} \\ \frac{-3 \sin \theta + \sin 3\theta}{16\sqrt{10}} & \frac{\cos \theta - \cos 3\theta}{16\sqrt{15}} & \frac{-5 \sin \theta - \sin 3\theta}{16\sqrt{6}} & \frac{15 \cos \theta + \cos 3\theta}{16} \end{pmatrix}. \quad (\text{A7})$$

The generalization of equation (A4) to arbitrary multipoles is obvious.